Supplementary Information

Selective Nucleation and Targeted Deposition Effect of Lithium in a Lithium-Metal Host Anode

Yun Zhao,[a] Bingbing Chen,[b] Shuhui Xia,[a] Jianyong Yu,[c] Jianhua Yan*[ac] and Bin Ding*[c]

[a] Key Laboratory of Textile Science & Technology of Ministry of Education, College of Textiles, Donghua University, Shanghai 201620, China.

[b] Department of Energy Science and Engineering, Nanjing Tech University, Nanjing, 210000, Jiangsu Province, China.

[c] Innovation Center for Textile Science and Technology, Donghua University, Shanghai 200051, China.

***Corresponding authors**: Jianhua Yan, E-mail: yanjianhua@dhu.edu.cn

Bin Ding, E-mail: binding@dhu.edu.cn

Experimental Section

Materials and Methods

Synthesis of MCNFs. To make stable PVA-BA-PTFE sol for electrospinning, 4 wt.% of BA solution by dissolving BA powders in deionized water and 15 wt.% of PVA solution by dissolving PVA powders (PVA 1788, Mw 83,000–85,000, Aladdin) in the deionized water at 90 °C for 3 h with a constant stirring rate were first prepared separately. Then, the BA solution and the PVA solution were mixed together and stirred for 1 h. The BA amount was controlled as 3 μL per gram of the PVA solution. After that, the sol was prepared by adding PTFE (120 nm) water emulsion (60 wt.% of PTFE) in the mixture solution and was stirred for 3 h. The electrospinning was carried out with a feed rate of 1.5 mL/h, a voltage of 22 kV, and a distance of 18 cm from the needle to the drum collector. The humidity and temperature of the electrospinning chamber were 45 ± 5 % and 25 ± 2 °C, respectively. After electrospinning, the as-spun fibers were kept in a vacuum oven at 80 °C for 2 h to remove the remaining water. The films were then thermally treated at 280 °C for 2 h with air cycling to pre-oxidizing PVA, followed by calcined at 415°C for 4 h and at 1000 °C for 2 h in Argon gas (Ar) with a heating rate of 5 °C/min to obtain MCNF films.

Synthesis of CNFs: The solution was prepared by dissolving Polyacrylonitrile (PAN, Mw = 90000) powders (10 wt%) in the Dimethylformamide (DMF) for 2 h with a constant stirring rate. The electrospinning process was carried out with a feed rate of 1 mL/h, a voltage of 25 kV and a distance of 20 cm from the needle to the drum collector. The humidity and temperature of the electrospinning chamber were controlled at 45 ± 5 % and 25 ± 2 °C, respectively. After electrospinning, the as-spun PAN NFs were dried at 80 °C for 2 h under vacuum to remove the

remaining DMF. The films were then thermally treated at 280 °C for 2 h with air cycling to pre-oxidizing PAN. Lastly, the films were calcined at 1000 °C for 2 h in Argon gas (Ar) with a heating rate of 5 °C/min to obtain CNF films.

Material Characterizations. Morphology and elemental distribution of the MCNFs were examined by SEM (Hitachi S-4800) and TEM (JEM-2100F). Crystal structure characterization was investigated using Bruker XRD with Cu Kα radiation between 10-80°. The graphitization degree and defect characteristics of the MCNFs were checked by Raman. The surface areas and pore size distribution of the MCNFs were measured with Brunauer–Emmett–Teller analyzer (ASAP 2460, Micromeritics, Co. USA). The surface chemistry was characterized by using XPS (Escalab 250Xi). For the cycled electrodes, they were washed by DME for three times and dried in glovebox before testing.

DFT Calculations. The Vienna ab initio package[1] was employed to perform all Spin-polarization DFT calculations within the generalized gradient approximation using the Perdew-Burke-Ernzerhof formulation[2]. We chose the projected augmented wave potentials[3] to describe the ionic cores and take valence electrons into account using a plane wave basis set with a kinetic energy cutoff of 400 eV[4-5] (Fig. S27). Partial occupancies of the Kohn−Sham orbitals were allowed using the Gaussian smearing method and a width of 0.05 eV. The electronic energy was considered self-consistent when the energy change was smaller than 10^{-6} eV. In our calculation, the equilibrium lattice constants of graphene unit cell (a=b=2.463 Å and c=6.801 Å) were optimized. And the 7×8×1 supercells of graphene has been calculated with lattice parameters. Finally, the different F sites can be doped into graphene structure to model the F doping structures. A geometry optimization was considered convergent when the energy change was

smaller than 0.05 eV/Å. Grimme's DFT-D3 methodology[6] was used to describe the dispersion interactions among all the atoms in adsorption models. The vacuum spacing in a direction perpendicular to the plane of the structure is 15 Å. The Brillouin zone integration is performed using 3×3×1 Monkhorst-Pack k-point sampling for our structures. Finally, the adsorption energies (Eads) were calculated as Eads= Ead/sub -Ead -Esub, where Ead/sub, Ead, and Esub were the total energies of the optimized adsorbate/substrate system, the adsorbate in the gas phase, and the clean substrate, respectively. The Li-ions migration barrier energies were evaluated using the climbing nudged elastic band methods.

Electrochemical Measurements. All the electrochemical measurements were carried out using CR2025-type coin batteries, in which Celgard 2500 was used as separators, and 1 M $LiPF_6$ in ethylene carbonate (EC), dimethyl carbonate (DMC), and ethyl methyl carbonate (EMC) (1:1:1 v/v) was used as electrolytes. The Li@MCNF anodes were obtained by electroplating 10 mA h/cm^2 of Li at 0.5 mA/cm^2. For the symmetric cell tests, Li@MCNF were used as the working electrode and commercial Li-foils were used as the counter electrode. For Li@MCNF//NCA batteries, the NCA cathodes were fabricated by mixing NCA, carbon black and polyvinylidene fluoride together with a mass ratio of 8:1:1. The areal NCA loading was 7.0 mg/cm^2. The cycling performance were measured by LAND and NEWARE test systems. The cyclic voltammetry (CV) test was measured by a Bio-Logic VSP workstation, and the test voltage range was 2.7-4.3 V, the scan rate was 0.1 mV/s. All these tests were conducted at room temperature.

Porosity calculations of MCNFs: MCNFs were composed of pores and carbon skeletons. It is assumed that all the absorbed saturated solution could be filled into the pores, and then the porosity was calculated by the following formulas:

$$\emptyset_{pore1} = \frac{m_1 - m_0}{m_1} \quad (1)$$

$$\emptyset_{pore2} = \frac{m_2 - m_0}{m_2} \quad (2)$$

Where $\emptyset_{pore1}$ was the porosity of the MCNFs with saturated solution (%), $\emptyset_{pore2}$was the porosity of the MCNFs with oversaturated solution (%), m0 was the mass of the MCNFs without solution, m_1 was the mass of the MCNFs with saturated solution, m_2 was the mass of the MCNFs with oversaturated solution. Orange DMF was selected as the filling solution and the saturated state was judged by the complete penetration of the fibrous film surface. To ensure that there was no overflow around, a piece of white filter paper was placed next to the MCNF film. If the white filter paper was dyed by the colored solution, it could be judged as supersaturation.

Notes and references

1 G. Kresse and J. Furthmüller, *Comput. Mater. Sci.*, 1996, **6**, 15-50.

2 J. P. Perdew, K. Burke and M. Ernzerhof, *Phys.Rev. Lett.*, 1996, **77**, 3865-3868.

3 G. Kresse, *Phy. Rev. B*, 1999, **59**, 1758-1775.

4 G. Zhou, L. Yin, D. Wang, L. Li, S. Pei, L. Gentle, F. Li and H. Cheng, *ACS Nano*, 2013, **6**, 5367-5375.

5 J. Zhao and J. Ma, J. *Phy.Chem. C*, 2016, **43**, 25131-25141.

6 S. Grimme, J. Antony, S. Ehrlich and H. Krieg, *J. Chem. Phys.*, 2010, **132**, 154104-154119.

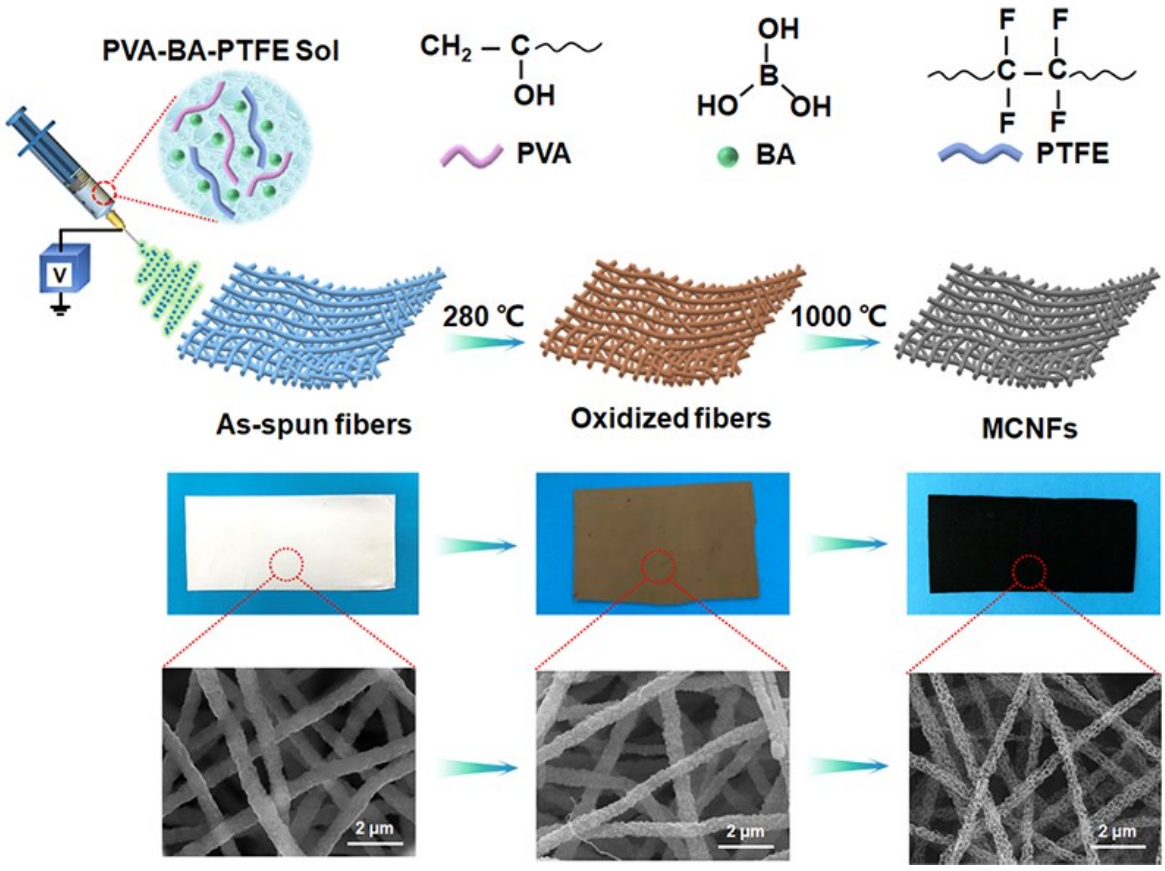

Figure S1. Manufacturing processes of the MCNF films and the corresponding morphology of the films in each step.

The MCNF films were synthesized with electrospinning followed by oxidation at 280 ℃ for 2 h and carbonization at 1000 ℃ for 2 h in Ar with a heating rate of 5 ℃/min. The dual micro-macro phase separations during the high-temperature pyrolysis brought a hieratical pore structure. It is noteworthy that no toxic chemicals or solvents were used to maintain the green synthetic method.

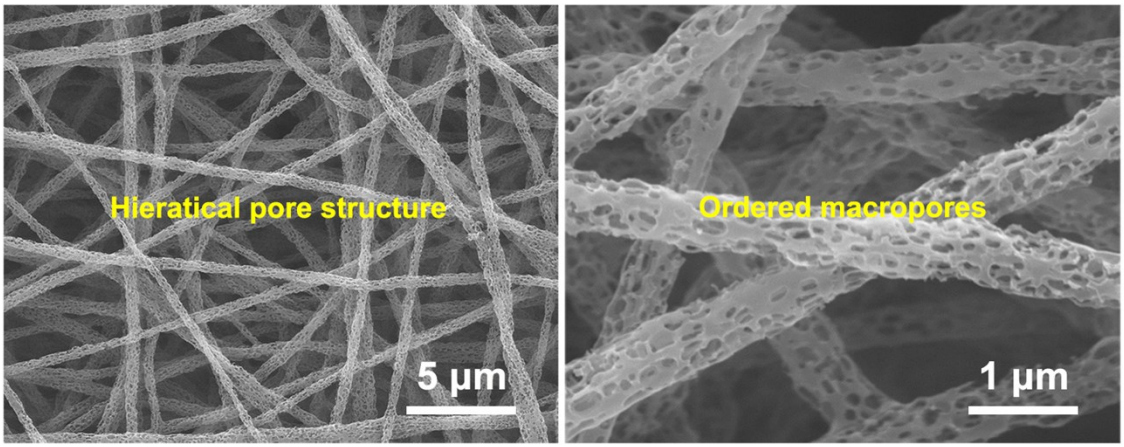

Figure S2. SEM figures of the MCNF films.

The pyrolysis of small-molecules of BA and PVA created meso- and micropores, while the decomposition of large PTFE NPs left ordered macropores.

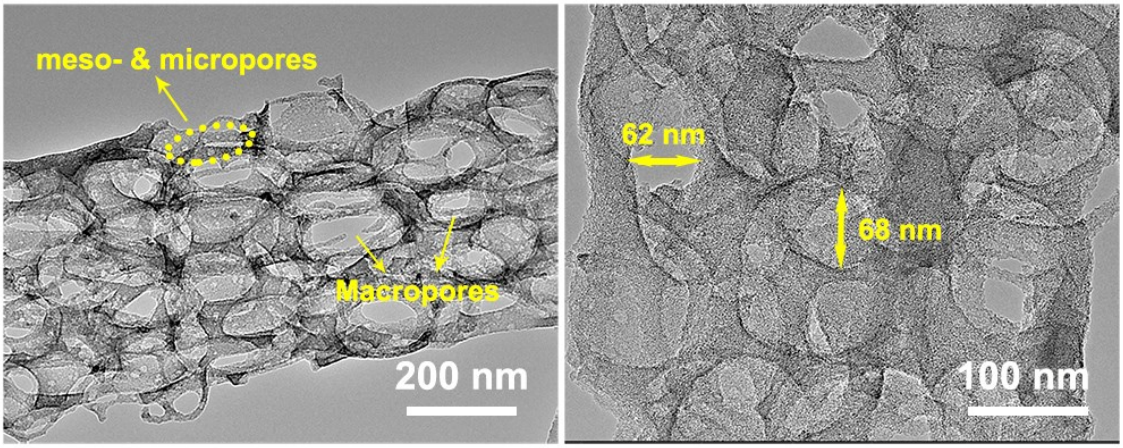

Figure S3. TEM figures of the MCNFs.

The MCNFs contained continuous macropores with pore sizes of > 60 nm throughout the full fibers.

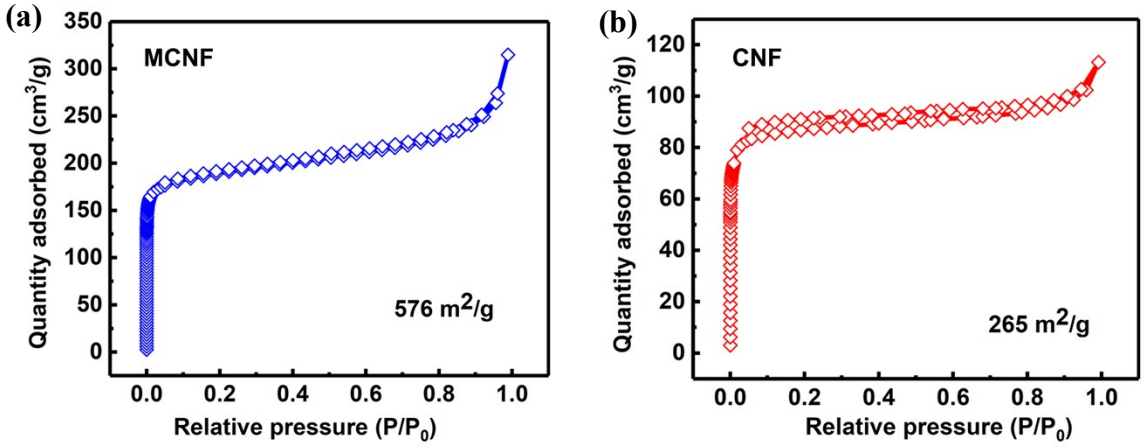

Figure S4. N_2 adsorption–desorption isotherms of (a) the MCNF film and (b) the CNF film.

For MCNF film, the N_2 absorption curve increased sharply when P/P_0 was <0.1 and >0.9, indicating there were large amounts of micro-, meso- and macropores in the MCNFs. These hieratical pores endowed the MCNFs with a high specific surface area of 576 m^2/g. The isotherms of CNFs exhibited typical type I and type IV isotherms with hysteresis loops, indicating that a large amount of micro-meso pores existed in CNFs, the specific surface area is 265 m^2/g.

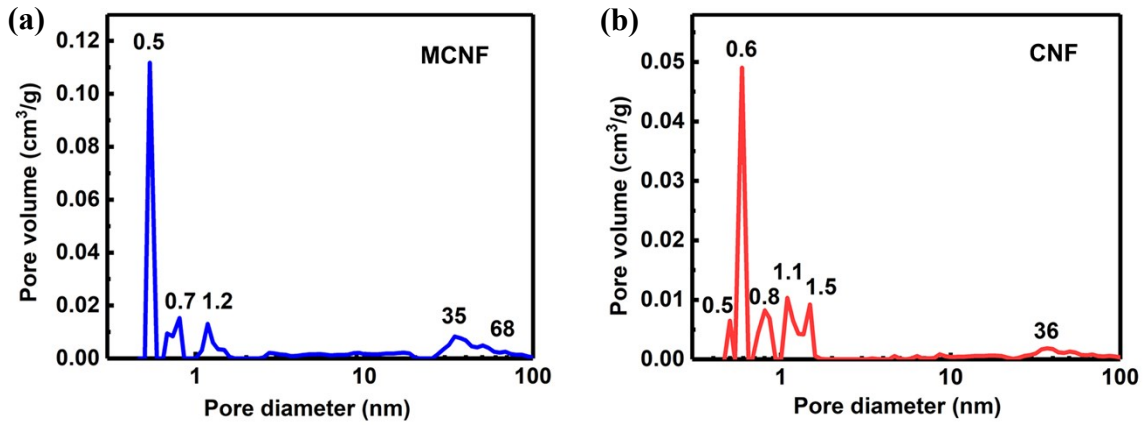

Figure S5. Pore size distribution of (a) the MCNF film and (b) the CNF.

For MCNFs, the micropore, mesopore and macropore sizes were concentrated at 0.5 nm, 35 nm and 68 nm, respectively. For CNFs, the micropore and mesopore sizes were centered around 0.6 nm and 36 nm.

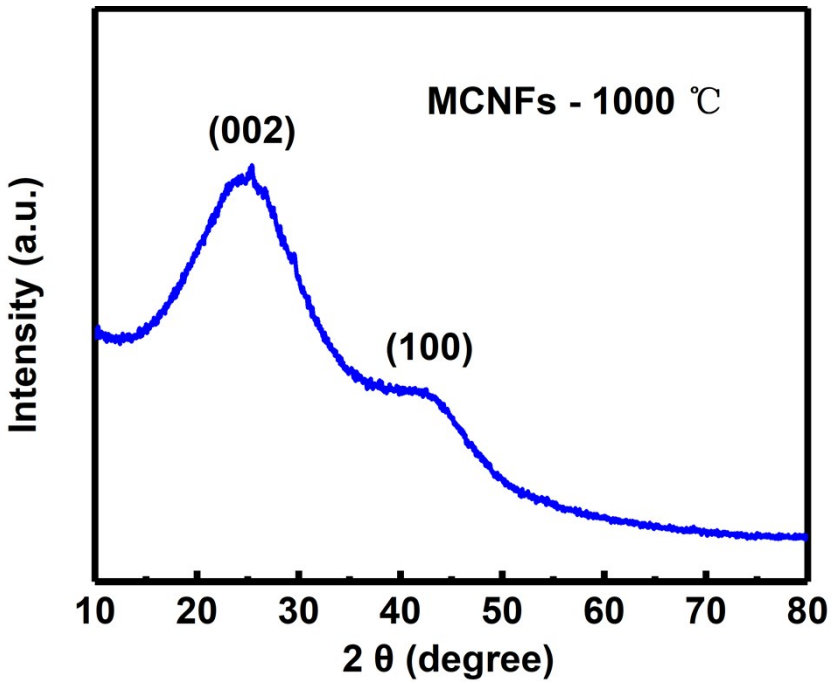

Figure S6. XRD test of the MCNFs-1000 ℃.

The spectra indicated the MCNFs had a mixed amorphous and graphitic structure.

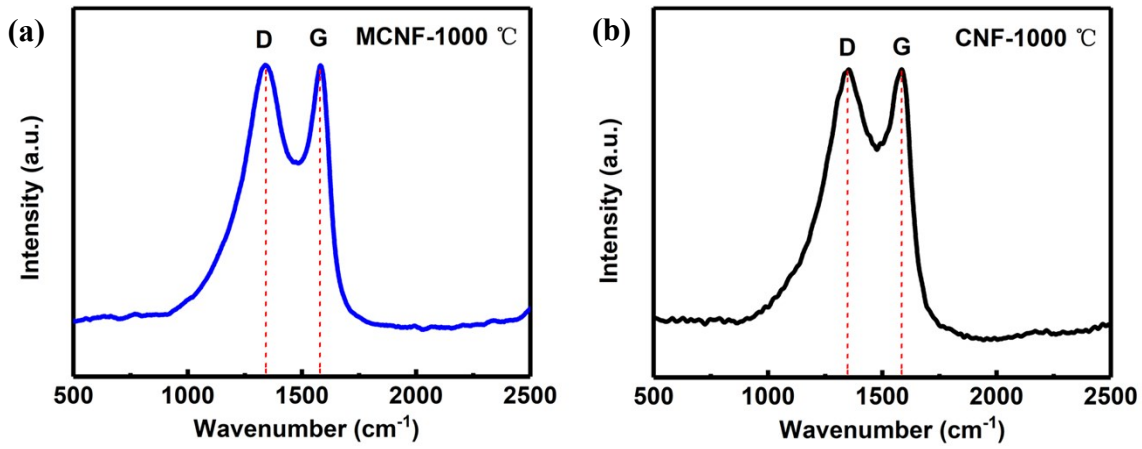

Figure S7. Raman spectrum of the (a) MCNF and (b) CNF film.

The D band (1355 cm^{-1}) and G band (1582 cm^{-1}) represented the defective and graphite structures, respectively. The ID/IG of MCNF and CNF film were both 1.0.

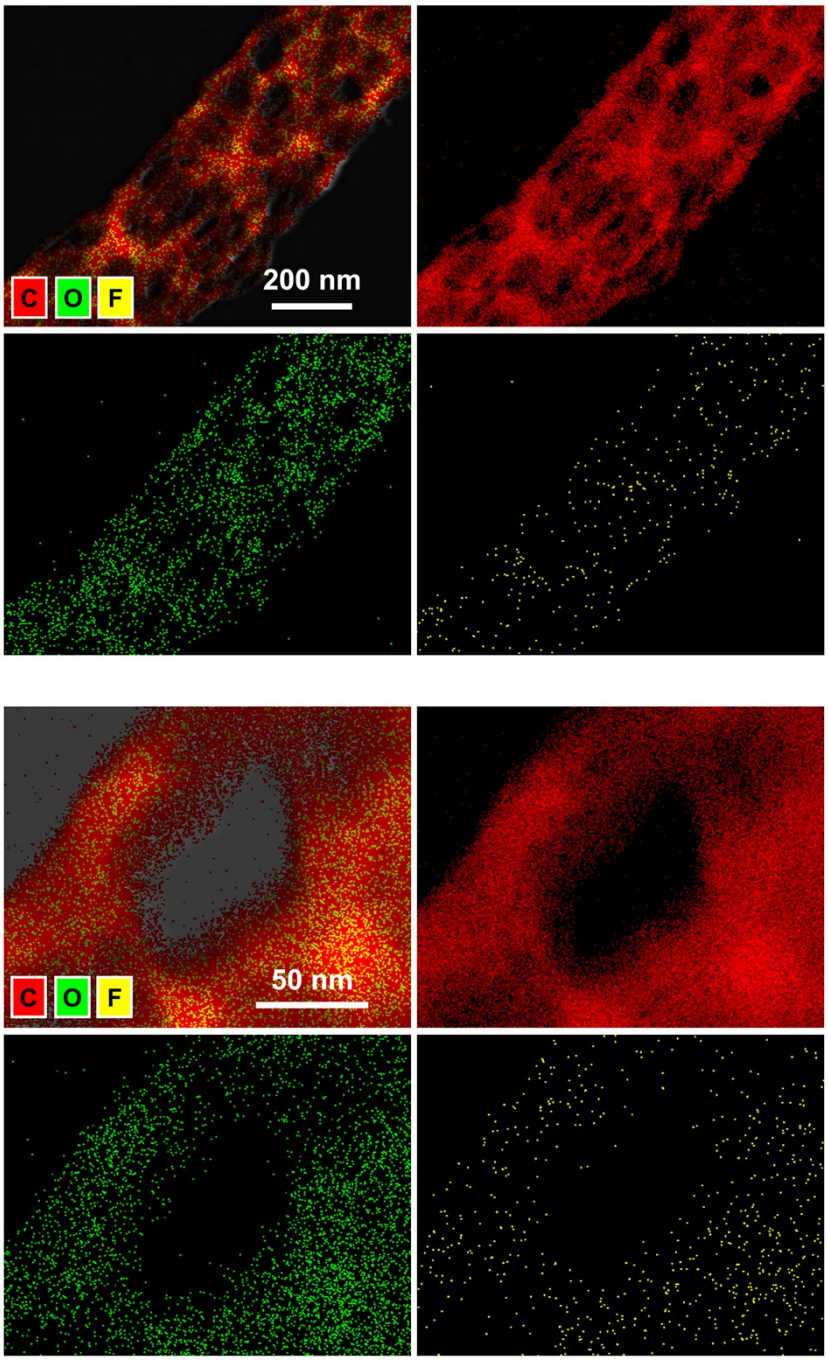

Figure S8. EDS mapping of MCNFs.

The EDS mapping exhibited that F-dopant were uniformly distributed in the MCNF matrix.

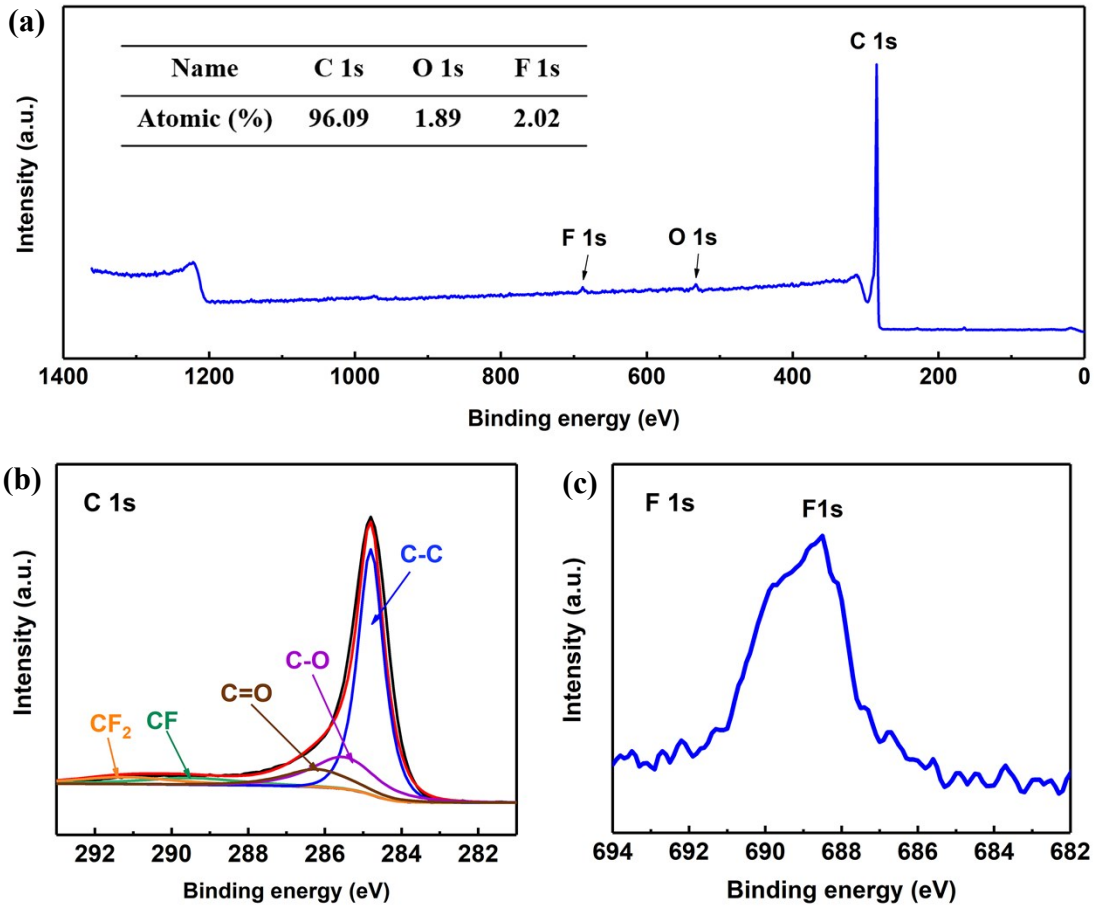

Figure S9. XPS characterization of the MCNFs.

(**a**) The atomic percent of C, O and F were 96.09 %, 1.89 % and 2.02 %, respectively. (**b**) C 1s and (**c**) F 1s spectra were presented. The peaks at 289.5 eV and 291.2 eV in the C 1s spectra were attributed to C-F and F-C-F groups, respectively, and the F 1s spectra at 688.2 eV further confirmed the formation of F-C bonds.

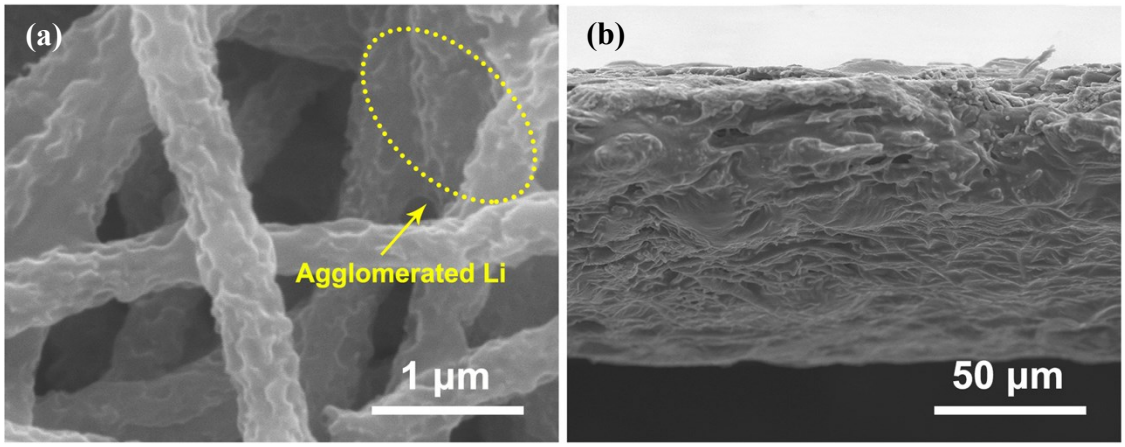

Figure S10. (a) Top view and (b) cross-sectional SEM images of the MCNFs host after being plated lithium with 15 mA h/cm^2.

A small part of Li began to accumulated at the fiber junctions, and the deposited Li-metal was always inside the 3D MCNFs current collector rather than aggregations on the upper surface.

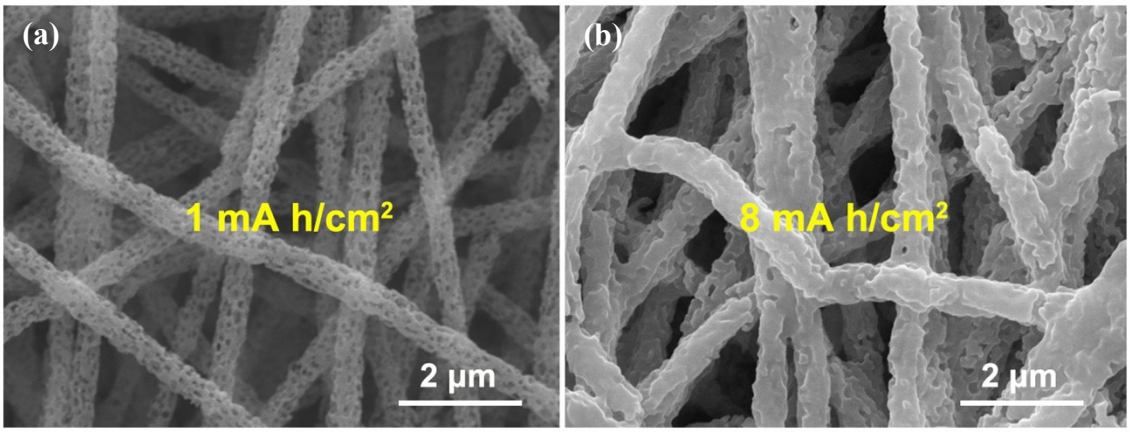

Figure S11. The top-view SEM images of the MCNFs host after being plated Li with (a) 1 mA h/cm^2 and (b) 8 mA h/cm^2 at a lower magnification.

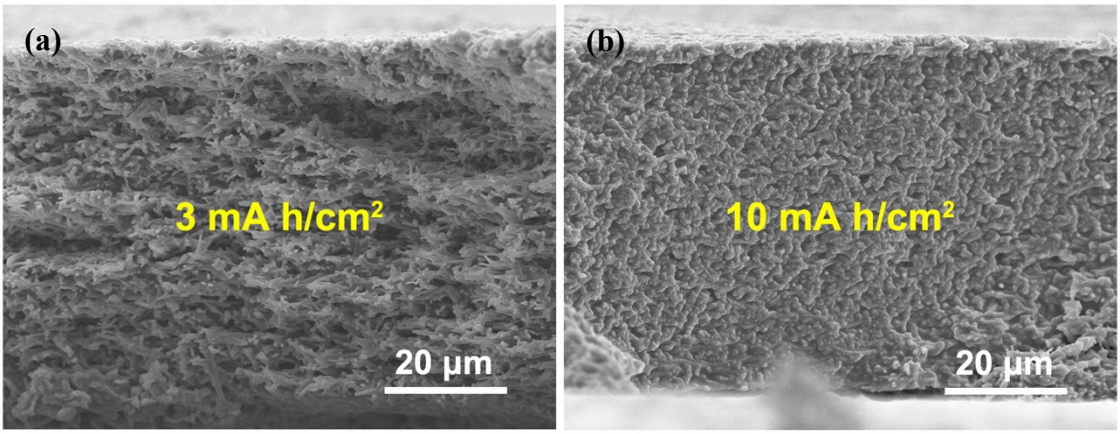

Figure S12. Cross-sectional SEM images of the MCNFs host after being plated Li with (a) 3 mA h/cm² and (b) 10 mA h/cm².

The Li@MCNFs anodes had a flat surface, and there were no Li-metal aggregations or Li-dendrites on the upper surface of 3D MCNFs host.

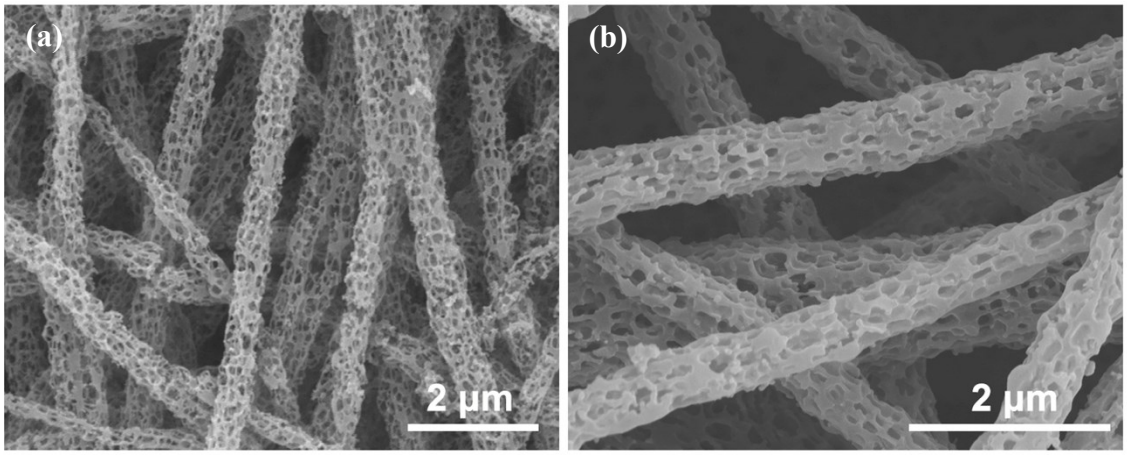

Figure S13. The top-view SEM images of MCNFs host after being plated Li of 10 mA h/cm^2 and then (a) completely being stripped, (b) stripped to 1 mA h/cm^2.

The fiber structure was well maintained.

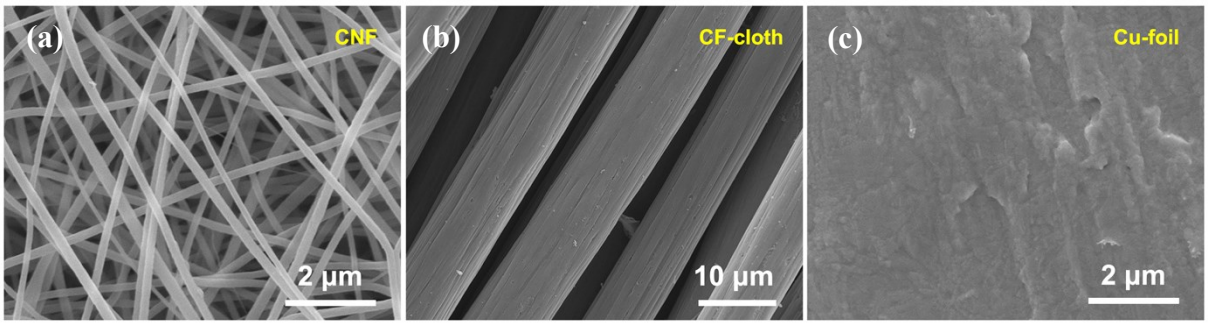

Figure S14. SEM images of (a) the CNF film (b) carbon fiber cloth and (c) Cu-foil.

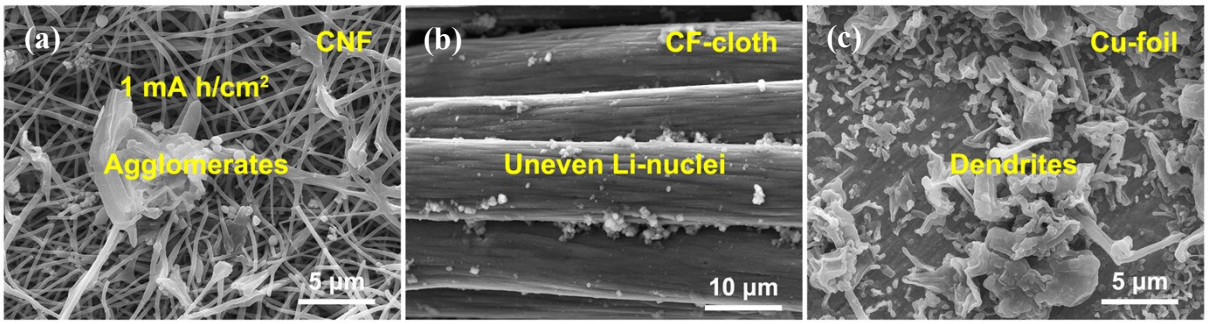

Figure S15. Li nucleation behavior on CNF, carbon fiber cloth and Cu-foil current collectors. SEM images of the (a) CNF, (b) CF-cloth and (c) Cu-foil current collector after plating 1 mA h/cm^2.

For the CNF and CF-cloth current collector, Li-agglomerates and nuclei were formed especially at the junctions of fibers, indicating an uncontrollable Li deposition behavior. For the Cu-foil current collector, there were obvious scattered large Li-nucleation deposits and dendrites.

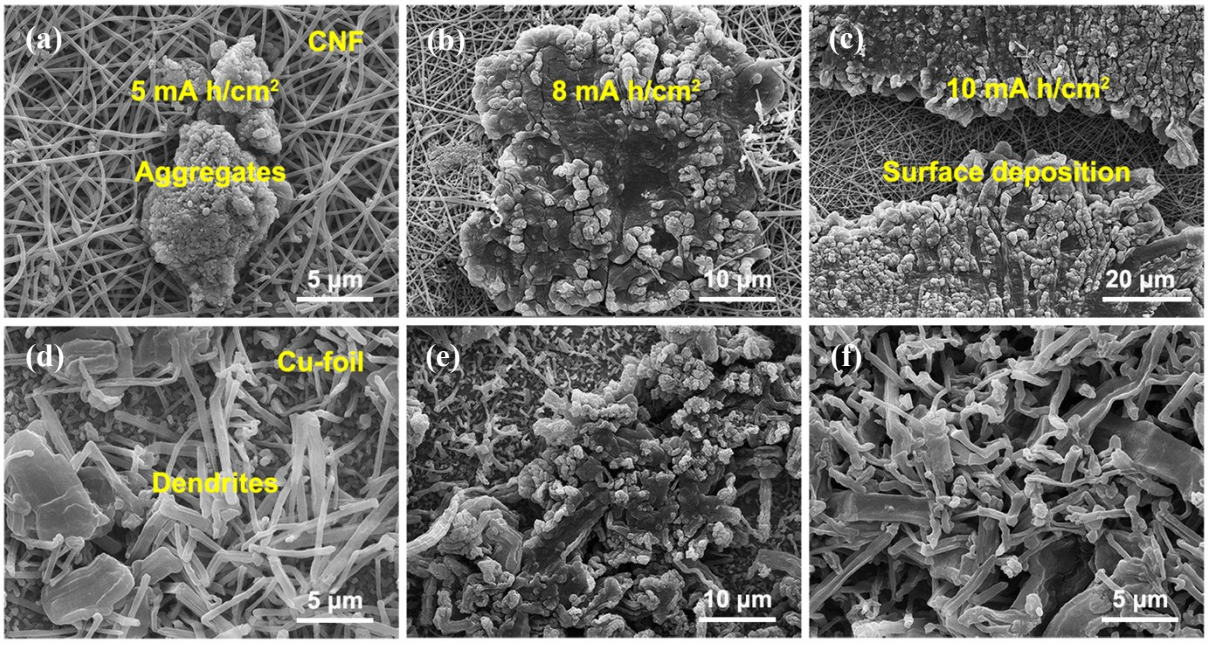

Figure S16. Li deposition behavior on CNF and Cu-foil current collectors. SEM images of the CNF and Cu-foil current collector after plating (a, d) 5 mA h/cm^2 (b, e) 8 mA h/cm^2 and (c, f) 10 mA h/cm^2.

As the deposition capacity increased, for CNF current collector, Li began to accumulated on the top and blocked inward ion-transport pathways, rendering the carefully designed 3D porous host structures became failure. For Cu-foil current collector, mossy Li and dendritic Li were significantly increased, which would increase the consumption of electrolyte and amounts of residual dead Li.

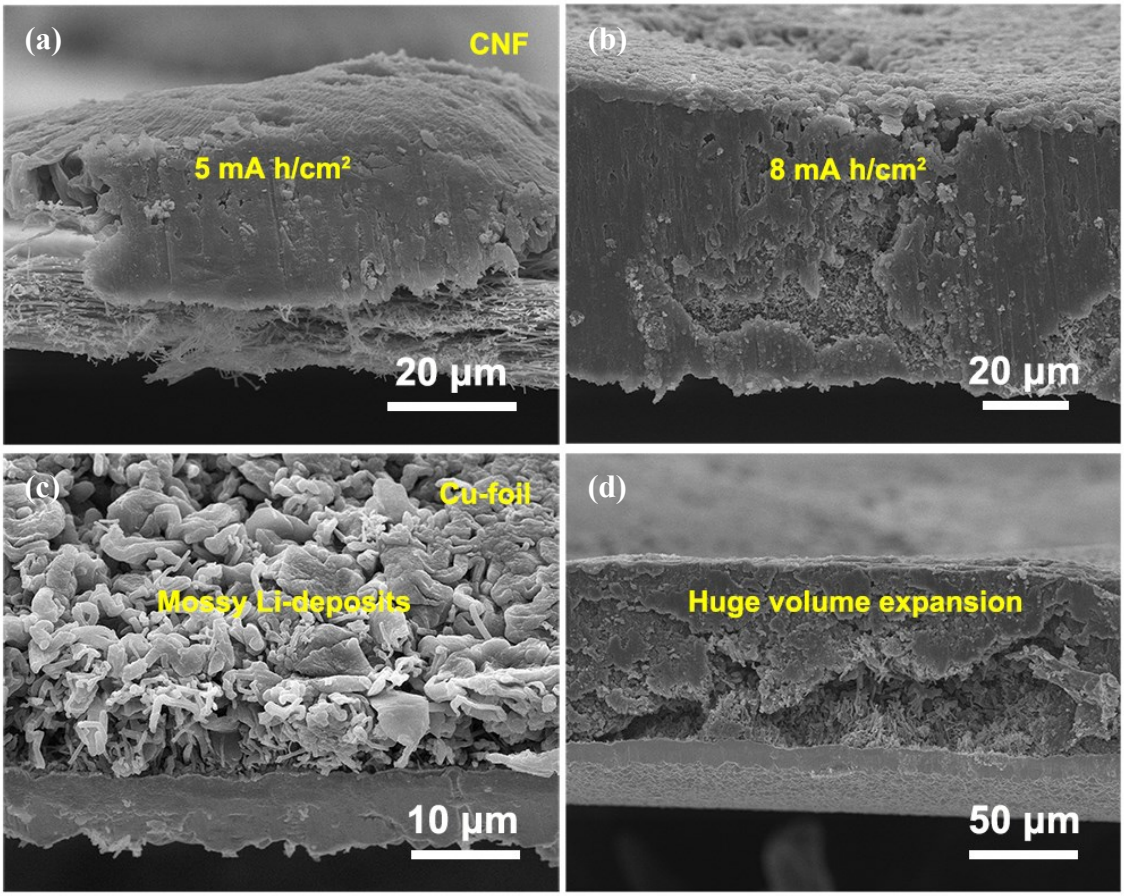

Figure S17. SEM images of the CNF and the Cu-foil current collectors after being plated Li with (a, c) 5 mA h/cm^2 and (b, d) 8 mA h/cm^2.

With the Li-capacity increased, both electrodes experienced huge volume expansion.

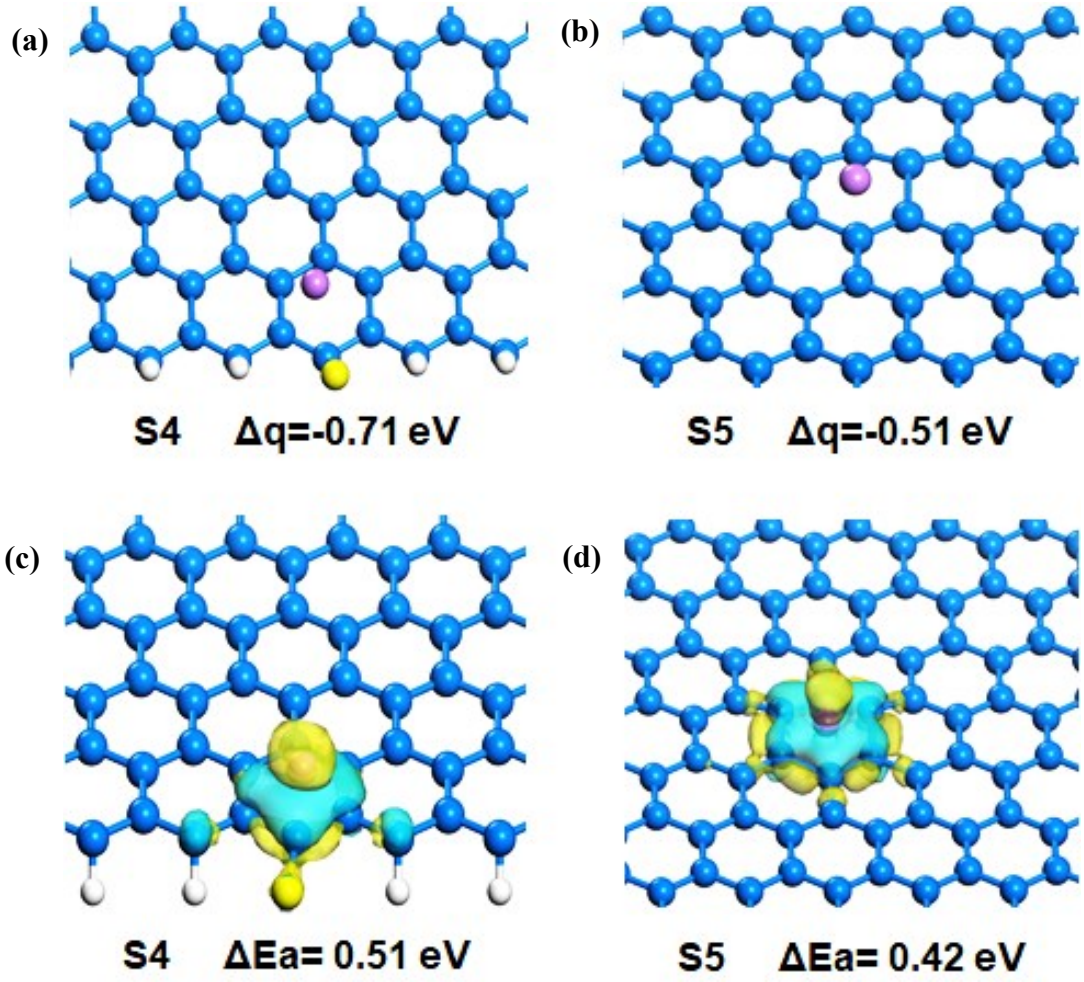

Figure S18. The Li-ion was absorbed by carbons with the edge F-doped defect (S4) and the ideal graphite structure (S5).

The adsorption energy of Li-ion by (a) carbons with the edge F-doped defect and (b) the ideal graphite structure. The charge density difference and Bader charge of Li absorbed in (c) carbons with the edge F-doped defect and (d) the ideal graphite structure.

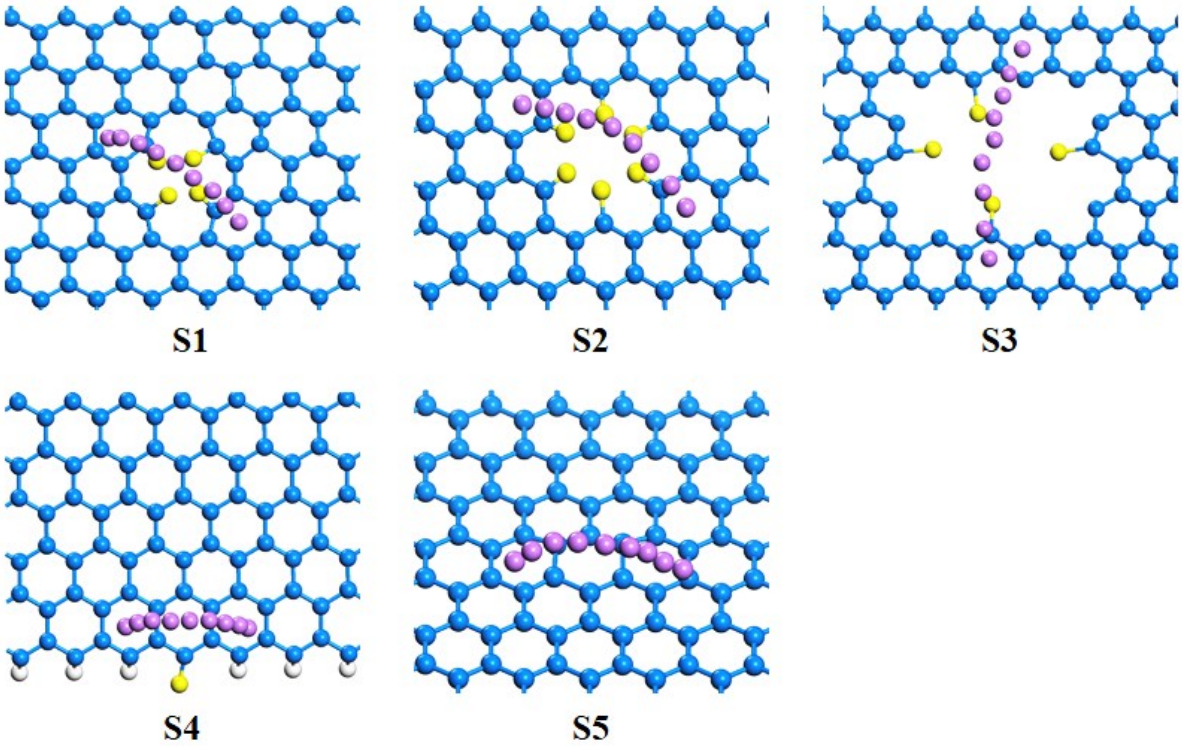

Figure S19. The migration behaviors of Li-ions on different defects and graphene structure.

Compared with the graphene model, both the F-rich macropore defects and F-doped edge defects showed much lower energy barriers for Li^+-migration. These results suggested that F-dopant could cooperate with the macropore defects to modify the charge density distribution and the adsorption free-energy barrier, thereby increasing the active sites in MCNFs and improving the battery rate performance.

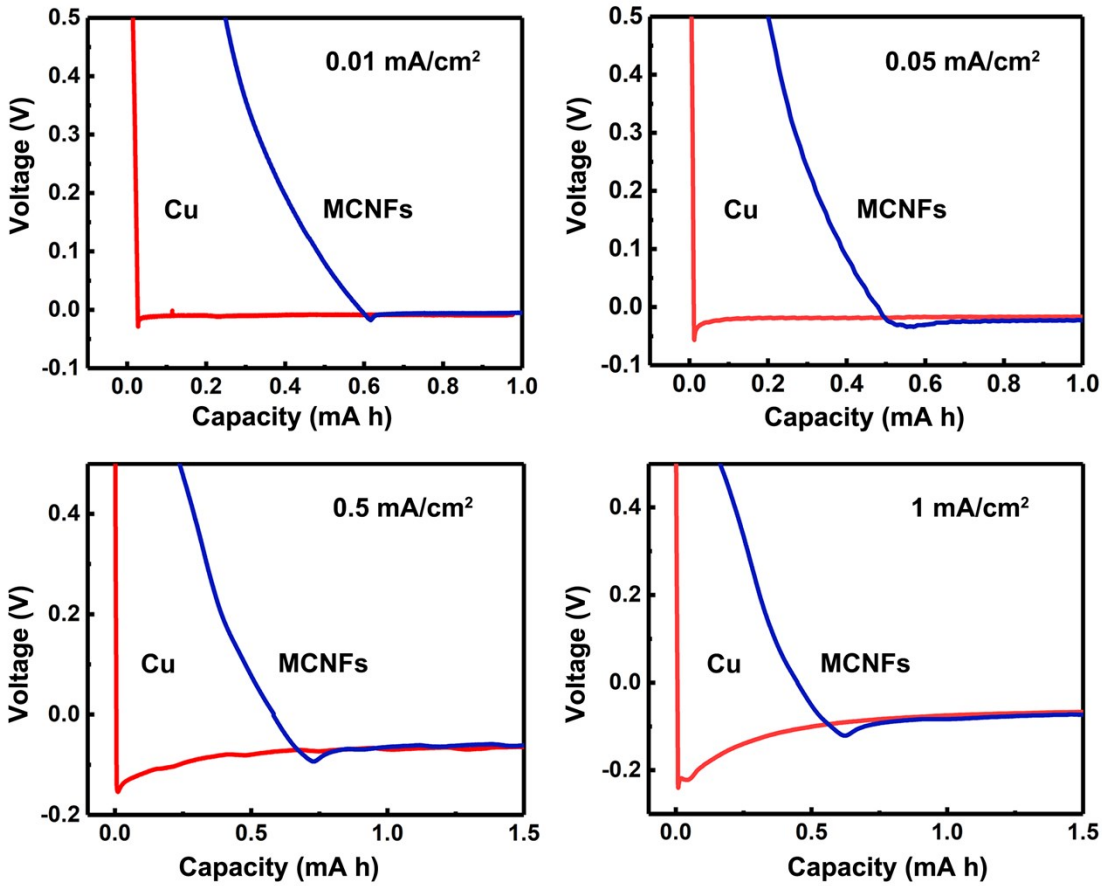

Figure S20. Nucleation overpotentials at different current densities.

With increment of the current density, the μ_n of the MCNF current collectors increased from 11 to 48 mV, which were always lower than that on the Cu-foil current collectors (from 20 to 173 mV). The Li-nucleation overpotential tests demonstrated the excellent lithiophilicity of the MCNF current collectors, which could induce a uniform Li deposition and thus dendrite-free Li-metal anodes.

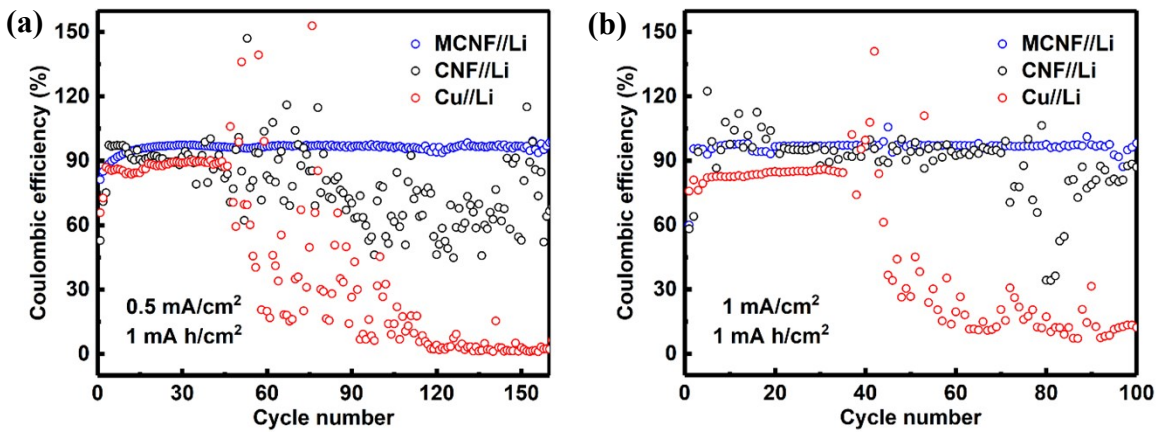

Figure S21. Coulombic efficiency evaluation of MCNF, CNF and Cu measured at (a) 0.5 mA/cm² for 1 mA h/cm² and (b) 1 mA/cm² for 1 mA h/cm².

The batteries were subjected to three "clean" cycles through galvanostatic charge/discharge at a low current density of 0.05 mA/cm² between 0 and 1 V to eliminate impurities.

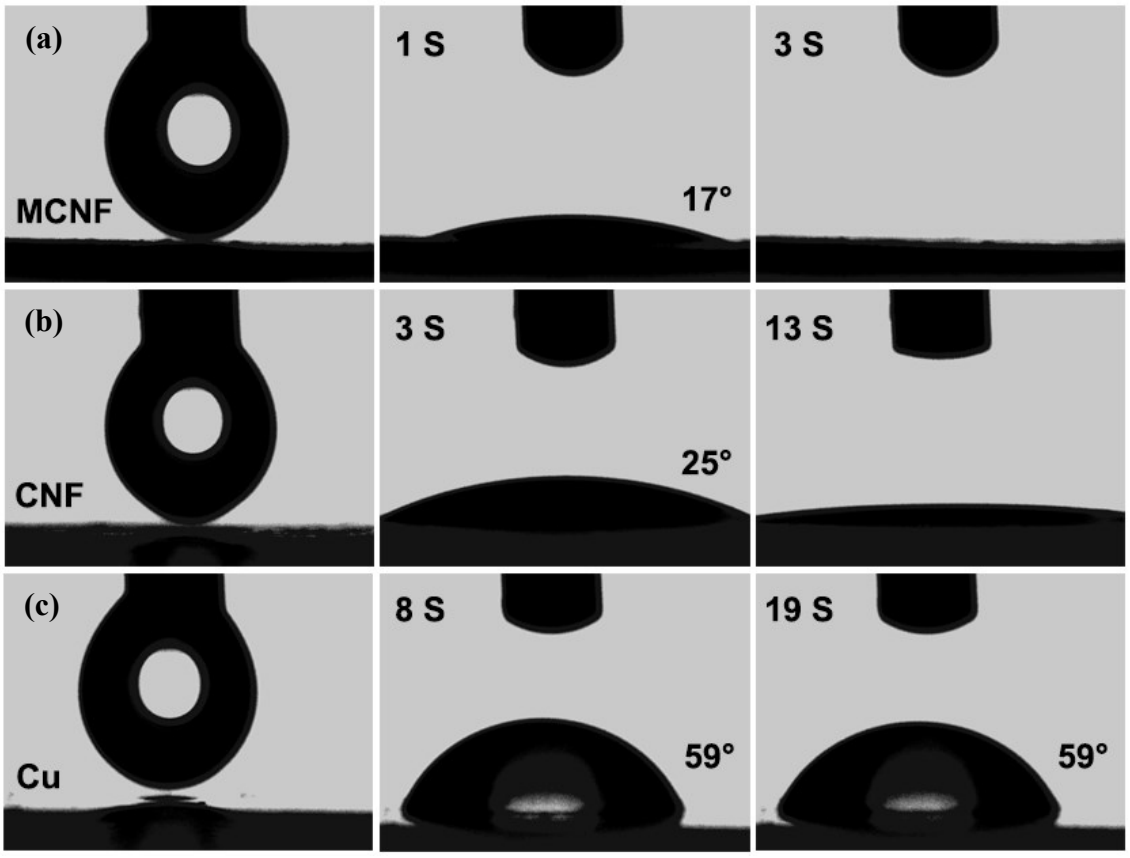

Figure S22. The contact angle of liquid electrolyte on (a) MCNF film, (b) CNF film and (c) Cu foil.

The MCNF film exhibited markedly enhanced electrolyte penetration ability and high electrolyte retention ability since when dipping the liquid electrolyte into the film, it could completely absorb them within 3 s.

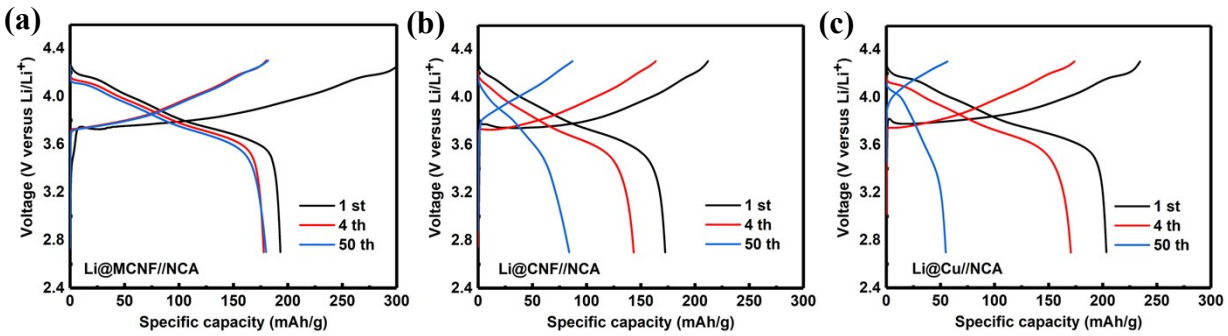

Figure S23. The corresponding charge/discharge curves of (a) Li@MCNF//NCA (b) Li@CNF//NCA and (c) Li@Cu//NCA cells at 1 C rate after the initial activation at 0.1 C for 3 cycles.

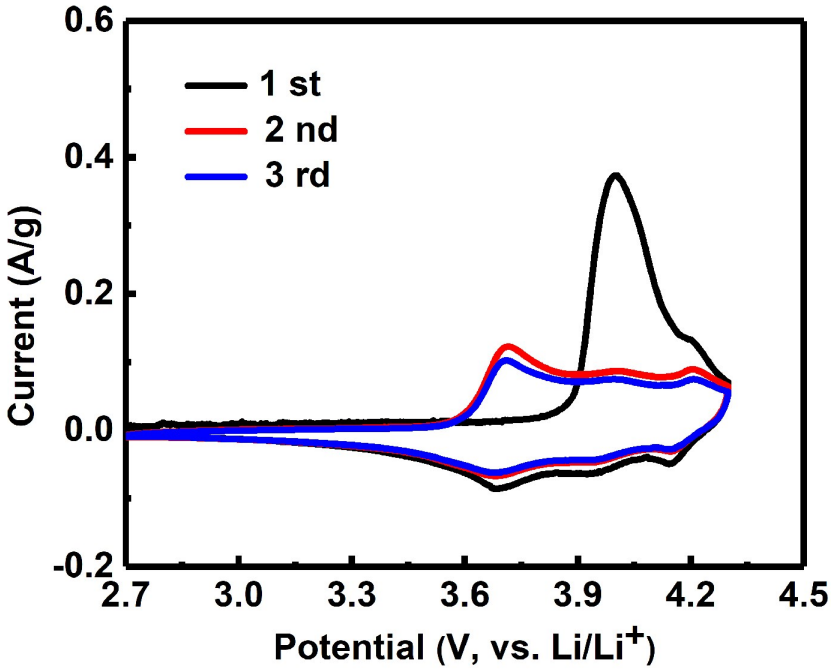

Figure S24. CV curves of Li@MCNF//NCA between 2.7 and 4.3 V (vs Li/Li^+) at a scan rate of 0.1 mV/s.

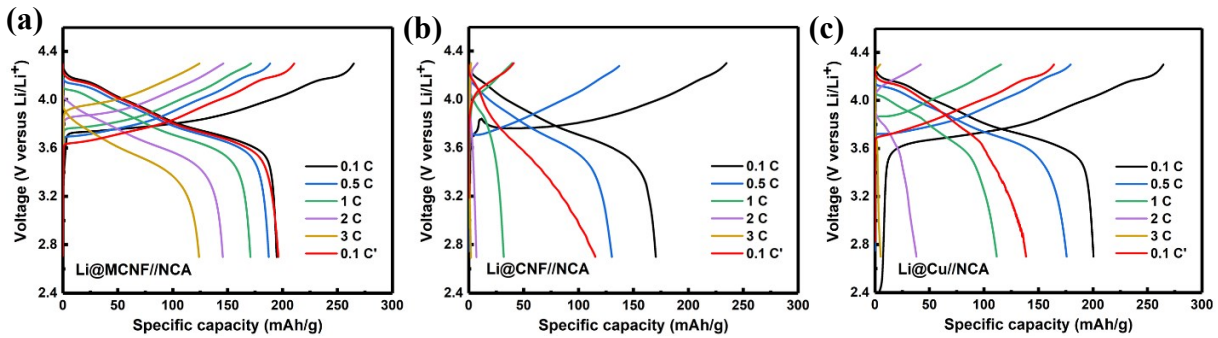

Figure S25. The corresponding charge/discharge curves of (a) Li@MCNF//NCA (b) Li@CNF//NCA and (c) Li@Cu//NCA cells.

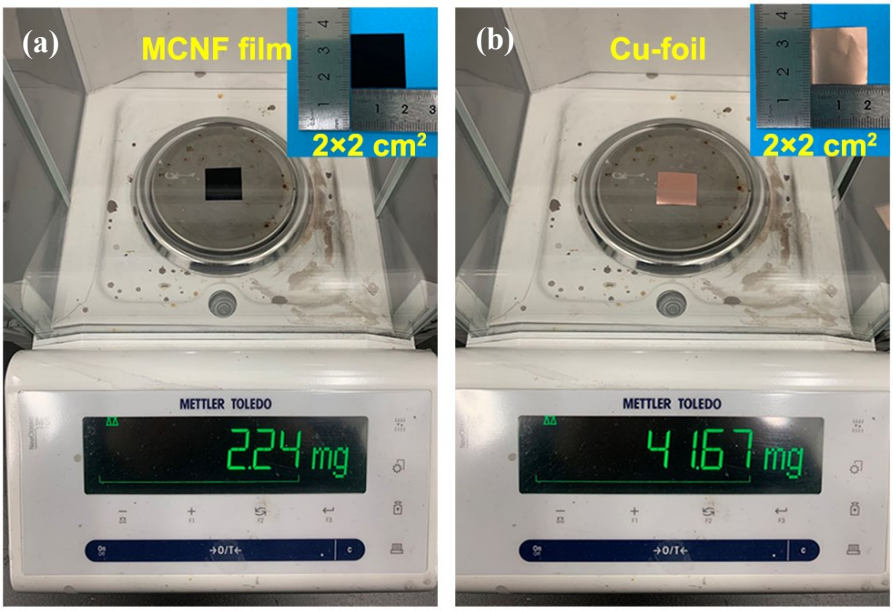

Figure S26. The weights of (a) the MCNF film and (b) the Cu-foil.

The side length of the square samples was 2 cm, corresponding to an area of 4 cm^2. The average thickness of the MCNF film and Cu-foil were 177.45 µm and 12.92 µm, respectively. Here, a thicker PCNF film was prepared for testing to minimize experimental errors. The thickness of the films was measured by a thickness gauge (CHY-C2, China).

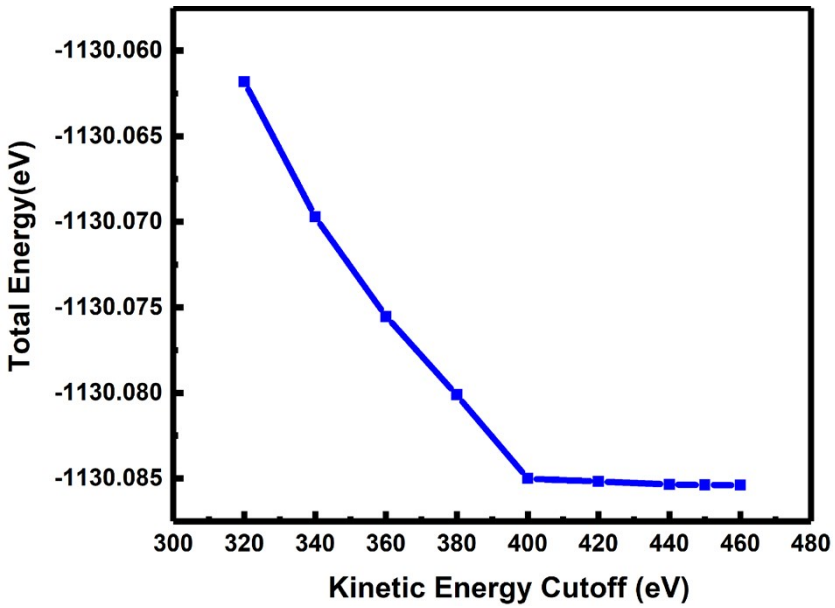

Figure S27. The relationship between kinetic energy cut-off and total energy.